

Phosphorylation disrupts long-distance electron transport in cytochrome *c*

Received: 18 July 2022

Accepted: 8 November 2022

Published online: 19 November 2022



Alexandre M. J. Gomila^{1,2,9}, Gonzalo Pérez-Mejías^{3,9}, Alba Nin-Hill^{4,9}, Alejandra Guerra-Castellano³, Laura Casas-Ferrer^{1,8}, Sthefany Ortiz-Tescari¹, Antonio Díaz-Quintana³, Josep Samitier^{1,2,5}, Carme Rovira^{4,6}✉, Miguel A. De la Rosa³, Irene Díaz-Moreno³✉, Pau Gorostiza^{1,2,6}✉, Marina I. Giannotti^{1,2,7}✉ & Anna Lagunas^{1,2}✉

It has been recently shown that electron transfer between mitochondrial cytochrome *c* and the cytochrome *c*₁ subunit of the cytochrome *bc*₁ can proceed at long-distance through the aqueous solution. Cytochrome *c* is thought to adjust its activity by changing the affinity for its partners via Tyr48 phosphorylation, but it is unknown how it impacts the nanoscopic environment, interaction forces, and long-range electron transfer. Here, we constrain the orientation and separation between cytochrome *c*₁ and cytochrome *c* or the phosphomimetic Y48pCMF cytochrome *c*, and deploy an array of single-molecule, bulk, and computational methods to investigate the molecular mechanism of electron transfer regulation by cytochrome *c* phosphorylation. We demonstrate that phosphorylation impairs long-range electron transfer, shortens the long-distance charge conduit between the partners, strengthens their interaction, and departs it from equilibrium. These results unveil a nanoscopic view of the interaction between redox protein partners in electron transport chains and its mechanisms of regulation.

Many electron transfer (ET) reactions occurring *in vivo* implicate pairs of proteins in which at least one of them is free to diffuse, like the small electron-carrying proteins plastocyanin, ferredoxin or cytochrome *c* (Cc)¹. Specific recognition and binding between proteins occur widely in biology. To reconcile an overall sustained and efficient ET process demands a high turnover rate. Therefore, the complex formed between redox proteins in the electron transport chain (ETC) must be transient, and balance specificity and binding strength^{2,3}. The recent direct experimental observation of electrochemically gated, long-distance ET between cytochrome *c*₁ (Cc₁, subunit of the cytochrome

*bc*₁) and Cc through the aqueous solution suggested that such tradeoff is achieved without direct contact, by molding the ionic distribution and electric field between their redox-active sites⁴. Thus, these redox protein partners might conciliate high specificity with weak binding, to keep the high turnover rate required by their biological function⁵.

Cc is a mitochondrial heme protein that exerts multiple functions, and its location depends on the cell condition^{6–10}. Under homeostasis, Cc localizes in the intermembrane mitochondrial space, transferring electrons from cytochrome *bc*₁ complex (Cbc₁, complex III) to cytochrome *c* oxidase (CcO, complex IV) in the ETC. Two binding sites for

¹Institute for Bioengineering of Catalonia (IBEC), The Barcelona Institute for Science and Technology (BIST), Barcelona, Spain. ²CIBER-BBN, ISCIII, Barcelona, Spain. ³Institute for Chemical Research–cicCartuja, Universidad de Sevilla, Consejo Superior de Investigaciones Científicas (CSIC), Sevilla, Spain. ⁴University of Barcelona, Department of Inorganic and Organic Chemistry, Institute of Theoretical Chemistry (IQTCUB), Barcelona, Spain. ⁵Department of Electronics and Biomedical Engineering, University of Barcelona (UB), Faculty of Physics, Barcelona, Spain. ⁶Catalan Institution for Research and Advanced Studies (ICREA), Barcelona, Spain. ⁷Department of Materials Science and Physical Chemistry, University of Barcelona (UB), Faculty of Chemistry, Barcelona, Spain. ⁸Present address: Laboratoire Charles Coulomb (L2C), UMR 5221 CNRS-Université de Montpellier, Montpellier, France. ⁹These authors contributed equally: Alexandre M. J. Gomila, Gonzalo Pérez-Mejías, Alba Nin-Hill. ✉e-mail: c.rovira@ub.edu; idadmoreno@us.es; pau@icrea.cat; migiannotti@ibecbarcelona.eu; alagunas@ibecbarcelona.eu

Cc on Cc₁ and CcO have recently been reported, a functional site (*proximal* site) enabling the correct orientation of redox centers to optimize the ET route, and a non-productive one (the so-called *distal* site) which is implicated in the turnover of Cc molecules^{11,12}. Cc also takes part in other redox reactions within mitochondria, including reactive oxygen species (ROS) scavenging, redox-coupled protein import via Erv1-Mia40 pathway, and reduction of p66Shc generating ROS⁸. Upon distinct stimuli, such as oxidative stress or DNA damage, Cc can relocate to several cell organelles, interacting with proteins governing cell life and death^{13–20}. Regarding oxidative stress, around 0.2–2% of the electrons involved in the ETC yield ROS via complex I (mainly), II, and III²¹. ROS have a dual role in cell signaling showing regulatory behavior at low levels and inducing apoptosis through oxidative stress at high ROS concentration. When mitochondrial production of hydrogen peroxide increases, Cc functions as a proapoptotic protein via its pseudo-peroxidase activity²². Around 15% of the Cc population is anchored to the inner mitochondrial membrane through binding to the lipid cardiolipin^{23,24}. The pseudo-peroxidase function of the cardiolipin-Cc complex is activated at high levels of hydrogen peroxide and leads to the release of the heme protein from the mitochondria into the cytosol where it triggers apoptosis^{25,26}. In mammals, Cc interacts in the cytosol with the apoptosis protease activating factor-1 protein (Apaf-1), to form the apoptosome and leading to downstream caspase activation and cell death^{8,27,28}.

These moonlighting Cc activities are tightly regulated by post-translational modifications (PTM)^{29,30}. Notably, phosphorylation occurs in physiological and disease conditions and is highly tissue specific. Up to five tissue-specific phosphorylation sites of Cc have been characterized in mammals, including Thr28, Ser47, Tyr48, Thr58 and Tyr97³¹. Phosphorylation of Cc has been described to exert a cytoprotective and antiapoptotic role by downregulating ETC flux, thereby preventing mitochondrial membrane potential hyperpolarization, decreasing ROS production, and avoiding caspase activation. Phosphorylation of Cc has also been related to several pathologies, such as ischemia/reperfusion injury, neurological disorders, and cancer progression³². Although phosphorylation mainly occurs on serine and threonine residues with high frequency, phosphorylation of tyrosine residues has a crucial role in the regulation of mechanisms directly relevant to mitochondrial and cancer signaling, such as metabolic homeostasis, differentiation, and proliferation^{33,34}. Among the two Cc tyrosine residues that can be phosphorylated *in vivo*, Tyr48 residue is located at the Ω -loop in the vicinity of the heme cleft, whereas Tyr97 lays far from the heme cleft in the C-terminal α helix of Cc. Cc phosphorylated on residue Tyr48 was primarily isolated from bovine liver tissue and it has been related to cancer³⁵. Moreover, it has been found that Tyr48 can be mutated by histidine, which causes a mild human disease—thrombocytopenia—that results in a lower level of blood platelets³⁶. Therefore, discerning the molecular mechanisms that regulate the function of phosphorylated Cc at position 48 is of great interest for understanding the role of Cc in pathology.

Functional studies revealed that Tyr48-phosphorylated Cc preserves the heme environment (no changes are observed in the Fe-Met80 absorption band at 695 nm) and that both Tyr48-phosphorylated and nonphosphorylated Cc species produced a hyperbolic kinetic response and the maximal turnover number of non-phosphorylated Cc was two times higher than that of phosphorylated Cc (3.7 s⁻¹ and 8.2 s⁻¹, respectively)³⁵. The technical difficulties to preserve the *in vivo* protein phosphorylation after purification, the large amount of phosphoprotein needed for structural and biophysical assays and the lack of information on specific Cc-Tyr48 kinases requires adopting other approaches to study this phosphorylated protein. Over the last years, some authors have developed engineered aminoacyl-tRNA synthetase systems that can incorporate O-phosphotyrosine. However, this approach presents multiple challenges as phosphotyrosine poorly penetrates the cells

due to its charge, it is unstable inside the cells and the incorporation efficiency by the aminoacyl-tRNA synthase is relatively low, producing a low yield of labelling (<5%) that is incompatible with single molecules techniques³⁷. A convenient approach is using phosphomimetic mutants for functional studies³⁸. The Cc Y48E mutant, in which Glu mimics the negative charge of the phosphate group, showed similar reaction kinetics to the non-phosphorylated Cc but presented a -45 mV midpoint redox potential shift. This mutation also inhibits the activation of caspase downstream signaling *in vitro*³⁹. Nevertheless, the Y48E mutation leads to *ca.* 20% decrease in the volume of residue Tyr48, whereas it is increased upon phosphorylation. Thus, using Y48E to mimic phosphorylated Y48 underrepresents volume-related effects⁴⁰. Therefore, the incorporation of a noncanonical amino acid that presents volume and charge values closer to those of phosphotyrosine is a better alternative. Among the different noncanonical amino acids that can be used to mimic Tyr-phosphorylation, *p*-carboxy-methyl-L-phenylalanine (*p*CMF) is one of the best substitutes, as it is stable, efficiently incorporated by *E. coli* cells, and preserves a similar volume than the phosphotyrosine residue⁴¹. This mutation does not affect the overall structure and heme iron environment as Tyr48-phosphorylated Cc (Supplementary Fig. 1)⁴². In terms of functionality, the Y48*p*CMF Cc shows lower binding affinity for the *distal* sites of Cc₁ and CcO, altering the diffusion pathway of Cc molecules through *Cbc*₁-CcO, thus modulating the ETC flux⁴². Finally, the Y48*p*CMF mutation effectively enhances peroxidase activity and induces an antiapoptotic function of Cc⁴².

Our recent observation of inter-protein long-distance ET between Cc₁ and Cc through the aqueous solution⁴ can be explained by the presence of a charge conduit at the active interface between the two proteins (Gouy-Chapman conduit). These results suggest that ET could occur already when the two proteins are approaching (i.e., in the encounter state) without the need of establishing a well-defined, static protein complex, thereby reconciling high specificity with weak binding, and allowing to keep the high turnover rate required in the ETC⁵. Within this scenario, the presence of a charge conduit is of paramount importance for a sustained electron transport. The spatial extent of the charge conduit was found to depend on the redox potential of the interacting proteins and on the charge distribution between them.

Here we aim to investigate the molecular mechanism of ET regulation by phosphorylation in Cc-Cc₁. We deploy an array of single-molecule, bulk, and computational methods to address this question in wildtype, phosphomimetic, and phosphorylated Cc. Our findings show that phosphorylation strengthens the interaction with Cc₁ (lower equilibrium dissociation constant—*K*_D—) and disrupts the Gouy-Chapman conduit associated with long-distance charge transport. These results could be of general significance for inter-protein ET, its regulation under diverse conditions in the cell, and the switching between multiple tasks.

Results

Long-distance ET between Cc-Cc₁ partners is impaired by Cc Tyr48 phosphorylation

The effects of Tyr48 replacement by the phosphomimetic *p*CMF in the inter-protein ET between Cc and the mitochondrial complex III, or *Cbc*₁, were studied using the cross complex between human Cc and the soluble domain of plant cytochrome Cc₁—which contains all residues of the physiological mature (without mitochondrial transit peptide) protein until Glu265, at which the C-terminal hydrophobic helix starts¹²—by means of electrochemical scanning tunneling microscopy (EC-STM)⁴. Cc and Cc₁ were immobilized on the probe and the sample electrodes of EC-STM, respectively, with their redox active sites facing the solution, thereby allowing protein interaction. Cc₁ was immobilized through its native N-terminal Cys10 to the Au(111) sample electrode of the EC-STM, and Cc or Y48*p*CMF Cc were anchored to the gold

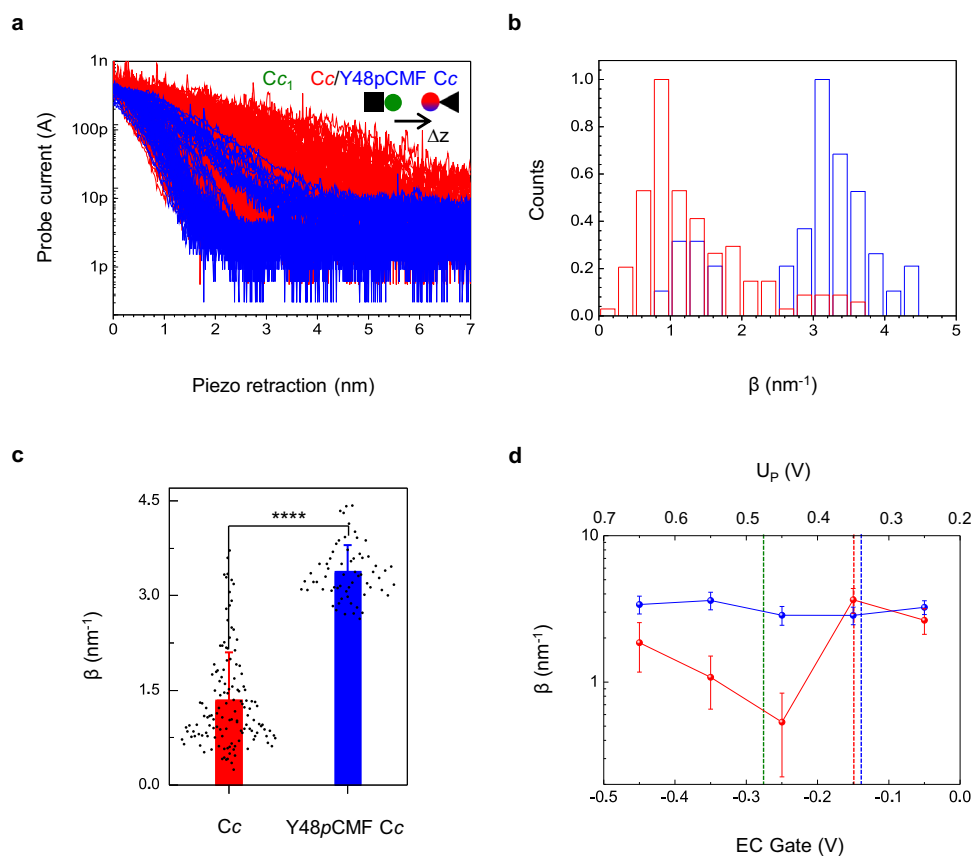


Fig. 1 | Current-distance electrochemical tunneling spectroscopy of Cc_1 -Cc.

a Ensemble of semi-logarithmic current-distance (I - z) curves during probe retraction, showing a more abrupt current decay for Cc_1 -Y48pCMF Cc. Sample and probe electrodes are represented by a square and a triangle, respectively. $U_s = -200$ mV vs. SSC and at constant bias of 800 mV. **b** Histograms of distance decay factors (β) quantified from individual curves in **a**. **c** Plot of the averaged β values (mean \pm s.d.) $\beta = 1.3 \pm 0.8$ nm $^{-1}$ for Cc_1 -Cc ($n = 103$ I - z curves from 2 independent experiments, red) and $\beta = 3.1 \pm 0.4$ nm $^{-1}$ Cc_1 -Y48pCMF Cc ($n = 64$ I - z curves from 2 independent experiments, blue), respectively, showing significant differences (two-sample t -test, t Statistic = 19.65, degrees of freedom = 195, **** $P < 0.0001$). **d** Averaged β

values (mean \pm s.d. of $n = 80$) vs. EC gate potential at 200 mV constant bias obtained for Cc_1 -Cc (red) and Cc_1 -Y48pCMF Cc (blue). The midpoint redox potentials for Cc_1 at the sample (0.276 V; green dashed line) and Cc or Y48pCMF Cc (red and blue dashed lines, respectively) at the probe are indicated, showing the β minimum for Cc_1 -Cc is located within the midpoint redox potentials of Cc₁ and Cc. Despite being redox-active at similar potential than Cc, Y48pCMF Cc did not display a β minimum within the measurement range. All experiments were performed in 50 mM phosphate buffer, pH 6.5. Initial current set point 0.4 nA. Averaged β values for Cc_1 -Cc (red) are reproduced from reference 4¹. Source data are provided as a Source Data file.

probe of the EC-STM through the C-terminal mutation E104C, thus facilitating the homogenous orientation of the proteins, while still preserving rotational freedom and good conductivity⁴³.

The experiments were conducted as described⁴⁴ in an electrochemical cell under bipotentiostatic control of the probe and sample electrodes versus an Ag/AgCl (SSC) reference electrode, spanning a potential range around the redox potentials of Cc_1 and Cc, and always keeping Cc_1 reduced (e.g. sample potential (U_s) = -0.20 V) and Cc oxidized (e.g. probe potential (U_p) = 0.60 V). These values yield a constant positive bias $U_{\text{bias}} = U_p - U_s = 0.80$ V by which the electrons are transferred from Cc_1 to Cc, in analogy to physiological ET.

Current-distance (I - z) electrochemical spectroscopy was conducted between Cc_1 -Cc and Cc_1 -Y48pCMF Cc in 50 mM phosphate buffer pH 6.5. By positioning the EC-STM probe over the sample at a current set point of 0.4 nA, and after a stabilization period, the feedback loop was briefly disconnected, and the probe current recorded while the piezoelectric scanner holding the probe was retracted 15 nm from the set point at 12 nm s $^{-1}$. Then, the feedback was restored, and the probe reengaged, allowing subsequent recordings at different areas of the sample. Faradaic leakage current was maintained below a few pA over the entire recording range through probe insulation⁴⁴. A nearly exponential current decay was observed in both cases from the initial current set point up to the distance-independent faradaic

leakage current. For Cc_1 -Cc the current decay spans several nanometers as previously reported⁴, while for Cc_1 -Y48pCMF Cc the current decays more abruptly, reaching leakage values 3 nm away from the set point (Fig. 1a). Fitting the exponential region of the curves yields the distance decay factor (β) distributions shown in Fig. 1b, which are centered at $\beta = 1.3 \pm 0.8$ nm $^{-1}$ for Cc_1 -Cc, and at $\beta_1 = 1.3 \pm 0.2$ nm $^{-1}$ and $\beta_2 = 3.1 \pm 0.4$ nm $^{-1}$ for Cc_1 -Y48pCMF Cc showing a bimodal distribution (Fig. 1c). Although β_1 values indicate that long-distance ET still takes place for a small population of recordings (up to 22%) in Cc_1 -Y48pCMF Cc, β_2 population doubling the β obtained for Cc suggests that the replacement of Tyr48 by the phosphomimetic pCMF causes a severe alteration of the inter-protein ET. The presence of the phosphomimetic group can affect inter-protein ET by perturbing the two main steps involved in the process. Namely, modifying intra-protein conduction pathways at the protein level or altering the interface between the two proteins and thus affecting the charge conduit. When we compared the β values between bare gold and either Cc or Y48pCMF Cc, we found no significant differences (Supplementary Fig. 2), thus indicating that the Y48pCMF mutation does not modify protein conduction, and that the changes observed in Fig. 1a, b may involve the charge conduit that is established between Cc_1 and Cc.

Electrochemical gating experiments were conducted for the Cc_1 -Y48pCMF Cc interaction. We recorded I - z plots at different probe and

sample potentials keeping the bias constant. The potential of the reference electrode was adjusted to modulate the gate voltage in analogy to the gate electrode in a field effect transistor. As the EC-STM probe is grounded in our STM electronic configuration, the EC gate corresponds to $-U_s$ at any given bias⁴⁵. For Cc_1 -Cc we have previously observed that β displays a marked potential dependence at a moderate bias of 200 mV. Averaged β values showed a minimum ($\beta = 0.5 \pm 0.3 \text{ nm}^{-1}$) at an EC gate potential of -0.25 V , which was located between the midpoint redox potentials of Cc_1 (0.28 V vs. SSC) and Cc (0.35 V vs. SSC), respectively (Fig. 1d, red curve). This potential-dependent effect allowed to measure current spanning more than 10 nm away from the departure set point and highlights the contribution of the redox sites in the ET between Cc_1 and Cc⁴. The β values of Cc_1 -Y48pCMF Cc do not depend on the EC gate within the considered redox potential window (Fig. 1d, blue curve), in striking contrast to Cc_1 -Cc. The midpoint redox potential of immobilized Y48pCMF Cc (0.36 V vs. SSC), is very similar to that of Cc (Supplementary Fig. 2), as previously reported⁴¹, and contrary to the Y48E substitution, which shows a $\sim 80 \text{ mV}$ reduction of its midpoint redox potential with respect to Cc³⁹. The redox potential values obtained are within the previously reported values for electron-transfer active Cc directly immobilized on an Au electrode^{46,47}. Therefore, Y48pCMF Cc maintains its redox activity but cannot be engaged in long-distance ET through the aqueous solution. This is likely due to an alteration in the charge conduit between the protein partners rather than coarse protein structural changes. Cc structure consists of five cooperative folding-unfolding units (foldons)⁴⁸ and its midpoint redox potential is very sensitive to protein folding and heme group coordination^{49,50}. As Met80 is located in the second most unstable foldon (foldon IV) of Cc, subtle alterations of Cc structure affect the Met80-Fe coordination bond and, therefore, the redox potential value. Indeed, several authors have demonstrated the important role of Met80-Fe coordination on Cc redox potential, as the loss of this bond shifts the redox potential towards negative values ($\sim 200 \text{ mV}$)⁵¹. Based on our voltammograms (Supplementary Fig. 2), we can rule out the hypothesis of partial or substantial denaturation of the protein after its immobilization on the Au(III) surface, since no voltammetric signal is observed at negative redox potential values.

To complement current-distance spectroscopy measurements, we studied current blinks in the static break-junction approach^{52,53} to measure the spontaneous interaction between protein partners (Fig. 2). By setting the current set point to $0.30 - 0.35 \text{ nA}$, and transiently disconnecting the feedback loop at a constant bias of 0.8 V , we recorded current vs. time (I - t) traces on Cc_1 -Cc and Cc_1 -Y48pCMF Cc interaction (Fig. 2a, red and blue, respectively). In the I - t curves, sudden jumps appear in the measured current (blinks), which are attributed to the spontaneous contact between the probe and the sample. The collected blink currents (I_{blink}), after subtracting the baseline current (I_{baseline}) were set to a common time origin (initial blinking time = 0) and plotted with the blinking lifetime in 2D-histograms (Fig. 2b). These 2D-blinking maps show the conductance dispersion of the partners' interaction. Taking the most probable conductance peak, we found that Cc_1 -Y48pCMF Cc interaction led to a significantly higher conductance ($P < 0.05$) (Fig. 2c). Gaussian fitting of main conductance peaks yields $G = (4.3 \cdot 10^{-6} \pm 9 \cdot 10^{-7}) \cdot G_0$ for Cc_1 -Cc and $G = (7.4 \cdot 10^{-6} \pm 5 \cdot 10^{-7}) \cdot G_0$ for Cc_1 -Y48pCMF Cc (with $G_0 = 2e^2/h$). In Fig. 2d, I_{blink} is plotted against its corresponding I_{baseline} showing that most probable Cc_1 -Cc interaction ($G = 4.3 \cdot 10^{-6} \pm 9 \cdot 10^{-7}) \cdot G_0$ can occur below the set point current (dashed line), thereby at longer distances than with Y48pCMF Cc, in agreement with I - z measurements.

Cc Tyr48 phosphorylation strengthens the Cc-Cc₁ interaction

Since EC-STM results suggest that Cc phosphorylation alters the interface between the two proteins, we further evaluated the inter-protein interaction using bulk and single molecule measurements.

We assessed the effect of Tyr48 replacement by the phosphomimetic pCMF on the interaction strength between Cc and Cc_1 by analyzing the forced unbinding between human Cc and the soluble domain of plant cytochrome Cc_1 using single molecule force spectroscopy with an atomic force microscope (AFM)⁵⁴. In addition, binding affinities of the Cc_1 -Cc complex were calculated from solution-based surface plasmon resonance (SPR) ensemble measurements, and the impact on Cbc_1 complex (complex III) activity was assessed in mammalian mitochondrial extracts.

To carry out single-molecule unbinding experiments, Cc_1 was immobilized on Au(III) substrates in a similar way as described for the EC-STM experiments. Either Cc or Y48pCMF Cc, both with the C-terminal mutation E104C, were conjugated to the maleimide group of a PEG₂₇ heterobifunctional crosslinker previously anchored to amino-functionalized AFM silicon probes. In the force spectroscopy measurements, the tip and substrate are approached and forced into contact up to a maximum force of 200 pN and then retracted away from the surface at constant velocity, in 50 mM phosphate buffer pH 6.5. The force-separation retraction traces at $1 \mu\text{m}\cdot\text{s}^{-1}$ velocity occasionally displayed unbinding events like those in Fig. 3a, which allows quantifying the force (F_r) and length (l_r) (see representative example in Fig. 3a inset) at which the contact is ruptured. The fact that the rupture length is maintained around 10–20 nm (Fig. 3b) indicates that protein unfolding is not significant, considering that the linker length is about 8 nm (monomer length of approx. 0.3 nm)^{55,56}, and the measured distances may be due to deformation and elongation of the proteins prior to dissociation. No correlation is found between F_r and l_r for neither Cc_1 -Cc nor Cc_1 -Y48pCMF Cc (Fig. 3b). For the pair Cc_1 -Cc, F_r is centered at $55 \pm 17 \text{ pN}$ (fitting a gaussian distribution) with a mean value of 75 pN (Fig. 3b, c). These relatively low rupture forces support the idea of the transient nature of the Cc_1 -Cc interaction. In contrast, Cc_1 -Y48pCMF Cc display higher unbinding forces ($P < 0.05$), centered at $77 \pm 24 \text{ pN}$ (gaussian fit) with a mean value of 91 pN (Fig. 3b, c).

We complemented these results with force-mediated dissociation kinetics studies. The lifetime of a bond sustained by weak noncovalent interactions decreases when subjected to force, which is conceptualized as force causing a tilt on the energy landscape, lowering energy barriers⁵⁷. The unbinding force generally depends on the loading rate, as theory predicts for many biological interactions like receptor-ligands bonds⁵⁸. In that case, the measured unbinding force corresponds to an individual point in a continuous spectrum of bond strengths. Therefore, we measured the rupture force at varying retraction velocities (from 0.5 to $4 \mu\text{m}\cdot\text{s}^{-1}$). To avoid transmission of the load through the polymer linker and bring high inaccuracy to the loading rate values, either Cc or Y48pCMF Cc were immobilized directly onto Au-coated probes through the thiol-Au chemistry. Here, the protein immobilization and orientation are comparable to those of the ECSTM experiments. The two proteins are then forced into contact and F_r and l_r are evaluated at different retraction velocities. These measurements only carry direct information of the kinetics of unbinding (not binding).

The force of Cc_1 -Cc unbinding is constant for the pulling velocities studied (contour maps F_r vs. l_r , Fig. 3d). In contrast, Cc_1 -Y48pCMF Cc unbinding becomes force resistant, and the unbinding force scales logarithmically with the pulling velocity and the loading rate (Fig. 3d). Cc_1 -Cc dissociation occurs at low forces independently of the pulling velocity (mean F_r vs velocity in log scale, Fig. 3e). This behavior is associated with two bodies being pulled apart during a near-equilibrium mode^{59–61}, in which complexes may have short lifetime and unbinding-rebinding is faster than pulling. This allows quick dissociation of the complex at biologically accessible loading rates and forces, in accordance with the requirement of a rapid turnover. In contrast, the rupture force between Cc_1 -Y48pCMF Cc depends logarithmically on the loading rate (r) (Fig. 3f), meaning that the measurements are done in a

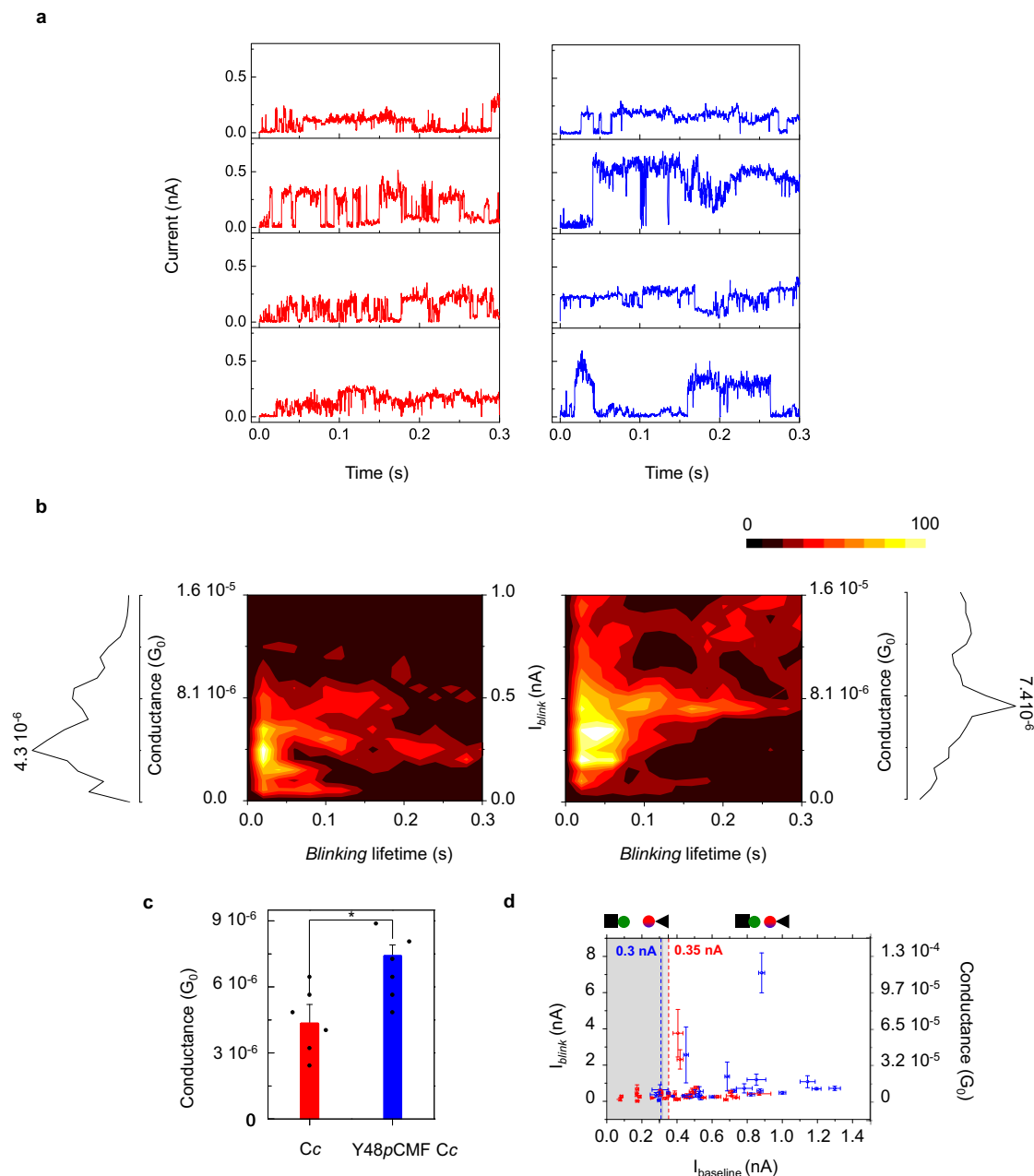


Fig. 2 | Blinking experiments. **a** Representative blinking recordings for C_{C1}-Cc (red) and C_{C1}-Y48pCMF Cc (blue). Blinks are shown as transient jumps of the current flowing between the two electrodes at a constant distance (imposed by initial current set point) and bias (800 mV). **b** Two-dimensional histograms of blink current (I_{blink}) and blink lifetime for C_{C1}-Cc (left, $n = 100980$ conductance values included) and for C_{C1}-Y48pCMF Cc (right, $n = 252193$ conductance values included). Counts have been normalized to a color scale, with 100 counts representing the maximum, and 0 representing the minimum. The corresponding conductance (G) profiles are shown. Baseline correction was applied in **a** and **b**. $G = I_{blink}/V_{bias}$ is used to obtain the conductance values. $G_0 = 2e^2/h = 77.5 \mu S$, with h the Planck constant and e the elementary charge. **c** Plot of the averaged G values from

gaussian fit of the most probable conductance peaks (mean \pm s.d.) $G = 4.3 \cdot 10^{-6} \pm 9 \cdot 10^{-7} G_0$ for C_{C1}-Cc (red) and $G = 7.4 \cdot 10^{-6} \pm 5 \cdot 10^{-7} G_0$ for C_{C1}-Y48pCMF Cc (blue), respectively, showing significant differences ($n = 6$ conductance values from 2 independent experiments, two sample t-test, t Statistic = 2.777, degrees of freedom = 10.00, * $P = 0.0195$). **d** Plot of I_{blink} against its baseline current ($I_{baseline}$) for a set of blinks of C_{C1}-Cc (red) and C_{C1}-Y48pCMF Cc (blue) (mean \pm s.d.). The dashed vertical lines indicate the corresponding current set points at which feedback was turned off. Sample and probe electrodes are represented by a square and a triangle, respectively. All experiments were performed in 50 mM phosphate buffer, pH 6.5. Source data are provided as a Source Data file.

kinetic regime (non-equilibrium bond rupture), as predicted by the Bell-Evans model based on a single transition state theory^{57,59,60,62}. The most probable unbinding force plotted against the loading rate on a log scale results in a straight line. Kinetic parameters can be obtained assuming that the energy barrier observed in dynamic force spectroscopy (DFS) remains rate limiting below the loading rate range tested. Following the Bell-Evans model^{57,59,62}, the rate of the molecular complex force-activated unbinding (k_u^o) and the

distance from the bound state to the barrier that is rate limiting for unbinding (x_u) can be calculated from a linear fit to the data only for the C_{C1}-Y48pCMF Cc pair ($k_u^o = 48 \text{ s}^{-1}$, $x_u = 0.31 \text{ nm}$). Overall, the DFS results indicate that the Y48pCMF mutation in Cc strengthens the interaction with C_{C1}, thereby hindering a fast turnover.

C_{C1}-Cc binding affinities were calculated from solution-based surface plasmon resonance (SPR) ensemble measurements. Protein binding affinities are commonly measured and described by the

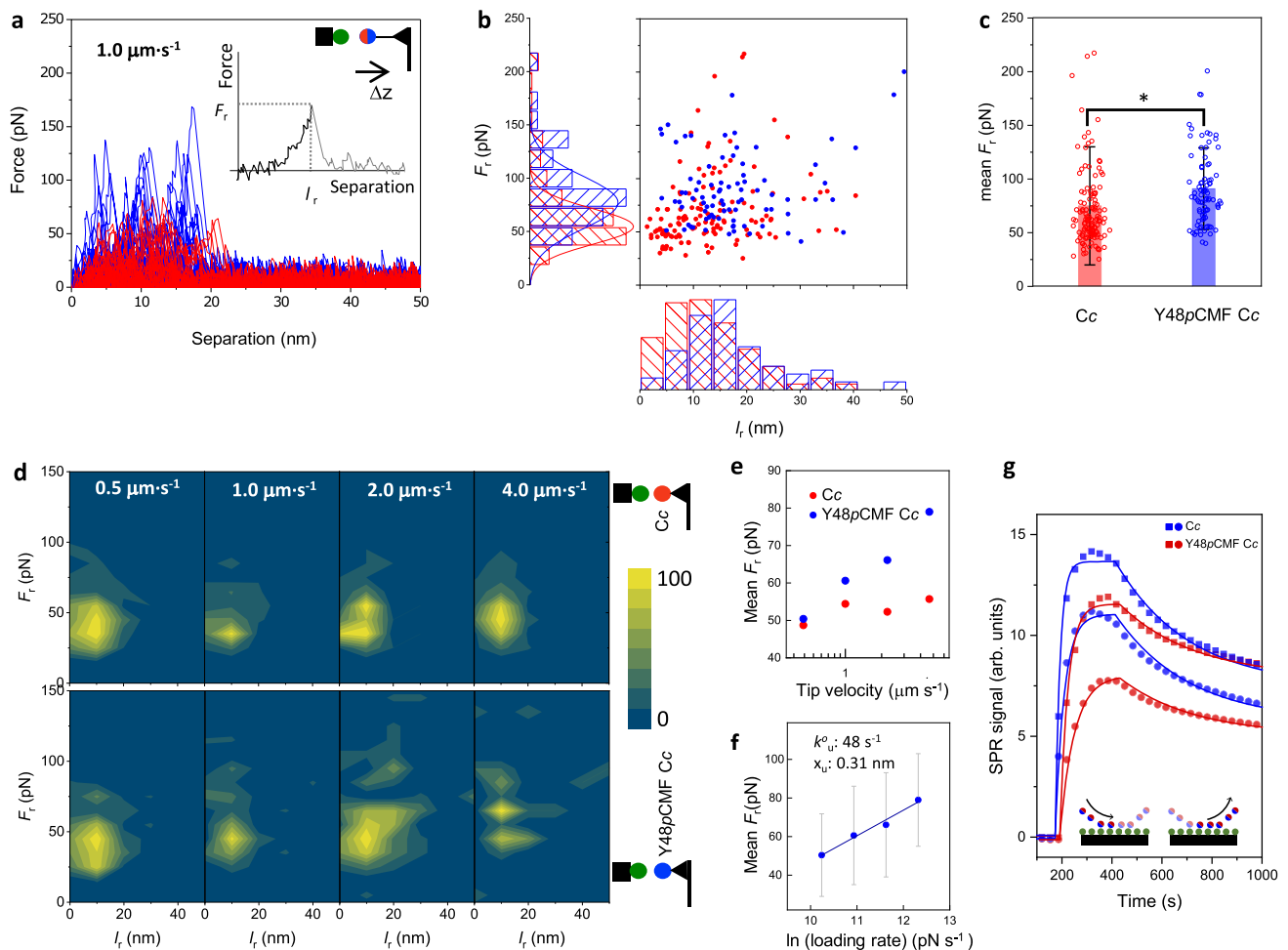


Fig. 3 | Unbinding between Cc_1 -Cc studied by AFM-FS single molecule and surface plasmon resonance (SPR) ensemble measurements. **a** Representative force-separation unbinding events upon tip retraction at $1 \mu\text{m}\cdot\text{s}^{-1}$ for Cc_1 -Cc (red) and Cc_1 -Y48pCMF Cc (blue), when Cc_1 is directly anchored to Au(111) and Cc is anchored to the AFM tip through a PEG₂₇ linker. The inset shows the parameters F_r and l_r , that are collected from each curve and displayed in **b** as F_r vs. l_r with the corresponding histograms in each axis. F_r distributions are fitted to a Gaussian. **c** Plot of the averaged F_r values (mean \pm s.d.) for Cc_1 -Cc ($n = 134$ force-separation curves from 2 independent experiments, red) and Cc_1 -Y48pCMF Cc ($n = 88$ force-separation curves from 3 independent experiments, blue), showing significant differences (two sample t-test, t Statistic = 2.34, degrees of freedom = 220, * $P = 0.02$). **d** F_r vs. l_r contour maps for the unbinding at different pulling rates (0.5 – $4.0 \mu\text{m}\cdot\text{s}^{-1}$) for Cc_1 -Cc (top, $n = 212, 185, 55$ and 226 for $0.5, 1.0, 2.0$ and $4.0 \mu\text{m}\cdot\text{s}^{-1}$,

respectively) and Cc_1 -Y48pCMF Cc (bottom, $n = 194, 83, 72$ and 97 for $0.5, 1.0, 2.0$ and $4.0 \mu\text{m}\cdot\text{s}^{-1}$, respectively), when Cc_1 is directly anchored to Au(111) and Cc is directly anchored to the Au-coated AFM tip. **e** Mean F_r vs. tip velocity (in log scale). **f** Average F_r (mean \pm s.d.) vs. \ln (loading rate) for the Cc_1 -Y48pCMF Cc unbinding fitted to a linear function (blue line) ($n = 194, 83, 72$ and 97 , for $28000, 56000, 112000$ and $224000 \text{ pN}\cdot\text{s}^{-1}$, respectively). Forced-activated unbinding parameters are calculated following the Bell-Evans model^{57,59,62}. All AFM experiments were performed in 50 mM PBS , $\text{pH } 6.5$. **g** Binding kinetics determined from SPR measurements. SPR sensograms obtained with $5 \mu\text{M}$ (squares) and $2.5 \mu\text{M}$ (circles) of Cc (red) and Y48pCMF Cc (blue) analyte and immobilized Cc_1 . Lines correspond to a simultaneous, global fit of the two curves to a one-site binomial model. Data is representative of a total of 16 spots. The binding assays were performed in 10 mM PBS , $\text{pH } 6.5$. Source data are provided as a Source Data file.

equilibrium dissociation constant (K_D), which evaluates the strength of biomolecular interactions (i.e., the greater the K_D value, the weaker the attraction between both protein partners). Fitting of the SPR curves for the interaction between Cc (WT and Y48pCMF) and Cc_1 to a 1:1 binding model (Fig. 3g) allows to obtain the association (k_{on}) and dissociation (k_{off}) rates for the interaction (Table 1). The calculated association rate k_{on} of Cc_1 -Y48pCMF Cc complex is nearly 2-fold larger than that of the Cc_1 -Cc complex, whereas the differences between spontaneous off-rate k_{off} values are small (but statistically significant, $P < 0.05$). Differences found between k_{off}^o values determined in single-molecule DFS experiments and spontaneous off-rates k_{off} values determined by SPR have been attributed to the complexity of the energy landscape that may cause high differences between the forced unbinding mechanism and the thermally activated one^{63,64}.

The differences in K_D ($k_{\text{off}}/k_{\text{on}}$) values between Cc and Y48pCMF Cc in complex with Cc_1 go along with the single molecule

force spectroscopy results, and agree with published NMR and ITC measurements⁴², demonstrating a stronger interaction force between Cc_1 -Cc when the Tyr48 residue is replaced by pCMF.

We further investigated if the observed differences in the unbinding forces and K_D values could modulate the mitochondrial complex III activity (Supplementary Fig. 4). The biochemical assay to study the complex III activity relies on following the changes in Cc redox state from oxidized to reduced, by recording the absorption spectrum of Cc at 550 nm . Our results with mammalian mitochondrial extracts showed that Y48pCMF Cc displays a 1.6-fold reduction ($P < 0.001$) of the net complex III activity ($0.28 \text{ nmol}\cdot\text{min}^{-1}\cdot\mu\text{g}^{-1}$ vs. $0.17 \text{ nmol}\cdot\text{min}^{-1}\cdot\mu\text{g}^{-1}$ for WT and Y48pCMF Cc, respectively). Such results support the hypothesis that the observed differences in unbinding forces and K_D values could be physiologically relevant in the modulation of the ET behavior of Tyr48-phosphorylated Cc.

Table 1 | Analysis of surface plasmon resonance (SPR) curves

Spot	Analyte	k_{on} ($M^{-1} s^{-1}$)	k_{off} (s^{-1})	K_D (M)
Cc ₁	Cc	$6.54 \cdot 10^3 \pm 8.8 \cdot 10^1$	$3.18 \cdot 10^{-3} \pm 5 \cdot 10^{-5}$	$5.27 \cdot 10^{-7} \pm 1.4 \cdot 10^{-8}$
	Y48pCMF Cc	$1.00 \cdot 10^4 \pm 1.57 \cdot 10^2$	$3.58 \cdot 10^{-3} \pm 6 \cdot 10^{-5}$	$3.57 \cdot 10^{-7} \pm 9 \cdot 10^{-9}$

Association rate (k_{on}) and spontaneous off-rate (k_{off}) constants and dissociation equilibrium constants (K_D) were calculated from the fits of SPR curves to 1:1 binding model. The errors reported are the standard errors derived from the fitting of the experimental data to a 1:1 binding model. R^2 are 0.9975 and 0.9954 for WT and Y48pCMF Cc fitting, respectively.

Cc phosphorylation disrupts the Gouy-Chapman conduit for long-distance ET with Cc₁

Long-distance currents between Cc and Cc₁ can be explained by a low ionic concentration in the aqueous gap between the two protein redox sites, compared to the solution bulk⁴. Cation depletion near the redox-active sites impairs charge screening in the solution and allows the electric field to extend several nanometers within the diffuse ionic Gouy-Chapman layer. To account for the changes in β observed when Tyr48 is replaced by the phosphomimetic pCMF in the EC-STM experiments, we performed molecular dynamics (MD) calculations of the pairs Cc₁-Cc (WT) and Cc₁-Y48pCMF Cc (phosphomimetic), as well as Cc₁-pY48 Cc (phosphorylated Tyr48: O-phospho-L-tyrosine) with charge -1 and -2. Note that the latter “true” phosphorylated Cc forms offer valuable insights as they are not yet experimentally accessible. The proteins were separated 3.2 nm with the redox active sites facing each other, in a solvent with explicit water molecules and 50 mM NaCl concentration (Supplementary Fig. 3a–d)

Cation depletion near the redox-active sites in the aqueous gap between the proteins is observed for Cc₁-Cc, and the concentration is nearly zero in the proximity of the redox active sites (Fig. 4a), in accordance with our previous studies⁴. In contrast, for Cc₁-Y48pCMF Cc an accumulation of cations is found around the proteins and in the region between them (Fig. 4b, h), likely due to the extra negative charge at position 48 that alters the surface electrostatic potential. This is reflected in the computed electrostatic potential in a 50 mM ionic concentration, which shows equipotential lines that extend between Cc and Cc₁ proteins, forming a conduit (Fig. 4c), but this is reduced between Y48pCMF Cc and Cc₁ (Fig. 4d). For Cc₁-Cc the space between both heme groups had the lowest average concentration of sodium ions (0.018 M) in comparison to Cc₁-Y48pCMF Cc (0.067 M). Thus, MD calculations show that the Y48pCMF mutation of Cc causes the disruption of the Gouy-Chapman conduit that has been associated to long-distance ET through the aqueous solution in agreement with EC-STM results. Interestingly, the phosphorylation of Tyr48 in native Cc may shift the electrostatic field even more than the Y48pCMF mutation, as evidenced when the computed average sodium concentration (average sodium concentration of 0.044 M for charge -1 and 0.052 M for charge -2, Fig. 4h, Supplementary Fig. 3e, f) and electrostatic potentials are obtained for pY48 Cc with charge -1 and -2 (Figs. 4e, f, h). In both cases, the equipotential lines do not extend between Cc and Cc₁.

We also performed Brownian dynamics (BD) simulations to calculate binding kinetics using the MD structures of Cc and Y48pCMF Cc complexes with Cc₁. For each computation, two curves are represented (Fig. 4i), corresponding to 4 independent pair-distances criteria for reaction, as reported previously⁶⁵. We estimated association rate (k_{on}) values at a distance of 0.6 nm as reaction criterion (vertical line in Fig. 4i). Cc and Y48pCMF Cc species show different behaviors across the simulation volume (expressed as distance cut-off dependencies of observables): i) the long-range attraction between Y48pCMF Cc and Cc₁ is larger than between Cc and Cc₁, and ii) below 12 nm, the estimated apparent k_{on} values for Y48pCMF Cc decay more steeply than in the case of Cc, probably due to bias of electrostatic steering. This matches the differences in force values found in DFS experiments,

indicating that the Y48pCMF mutation strengthens the interaction with Cc₁, as pointed out before. The ratio between the k_{on} values decreases hyperbolically with the distance, reflecting the impact of changes in the energetic landscape of interaction. The rate constant $k_{trigger}$ was set at the cut-off distance (2.5 nm) at which ET can be triggered in the EC-STM experiments. At the contact level, reckoned k_{on} for Cc₁-Y48pCMF Cc are ca. 10-fold larger than those estimated for Cc₁-Cc (Table 2, Fig. 4i). At the cut-off distance of 2.5 nm, $k_{trigger}$ values increase 2-3-fold in the trajectories corresponding to Cc₁-Y48pCMF Cc compared to Cc₁-Cc. In summary, Cc₁ attracts Y48pCMF Cc stronger than the WT Cc, even at long distances.

Discussion

Phosphorylation is one of the most prevalent mechanisms of regulation of protein activity. In particular, tyrosine phosphorylation plays a crucial role in cellular processes such as metabolism or cellular growth. Cc and its partner CcO are among the mitochondrial proteins whose function is highly regulated by phosphorylation. Cc phosphorylation has been suggested to perform a crucial role in regulating mitochondrial respiration and cell fate³⁰.

Tyr48 phosphorylation has been reported to affect the binding affinity of Cc towards its molecular partners, altering the diffusion pathway of Cc molecules through Cbc₁-CcO and affecting the ETC flux by partially inhibiting the mitochondrial respiration⁴². However, the molecular mechanism through which Cc phosphorylation impacts the ETC is unknown. The multimodal experiments on phosphomimetic Cc and calculations reported here show that upon phosphorylation the long-distance charge conduit established between Cc-Cc₁ is shut off and their interaction is strengthened and departed from binding/unbinding equilibrium in the measured conditions. Overall, these results are in full agreement with the consensus evidence published on the topic and unveil a nanoscopic view and mechanistic framework that offers deeper insights into the interaction between redox protein partners of the respiratory ETC.

Notably, these results indicate a regulatory advantage of using electrochemically gated, long-distance electron transport through the solution between redox partner proteins. Besides reconciling high specificity and electron transport efficacy with weak binding to keep high turnover rates⁴, the Gouy-Chapman conduit bearing reduced ionic density in the confined volume between the proteins can be externally controlled to reduce charge flow. When phosphorylated at Tyr48 (herein mimicked by replacement with pCMF), Cc sliding from Cbc₁ to CcO is impaired⁴². The stronger interaction between the partners upon phosphorylation was considered to hinder the Cc turnover (exchange with the partner) as it would lead to a frozen complex as concluded from calorimetry data and NMR spectroscopy results⁴². Note that our scanning probe microscopies experiments allow probing interactions at the single protein level, and in the case of EC-STM (*I*-*z* and blinking studies) it is possible to keep Cc₁ reduced, and Cc oxidized to mimic the physiological situation of ET from Cc₁ to Cc. Independent control of probe and sample electrochemical potential in the single molecule force spectroscopy AFM setup is more challenging^{66,67} and constitutes one aspect to improve experimentally in future studies.

We observe that electrochemically gated long-range ET is impaired in single-molecule experiments with phosphomimetic Y48pCMF Cc, with current decay distances reducing to half (to 3 nm or less, Fig. 1a–c) and abolishing EC gate potential control (Fig. 1d). MD simulations show that the negative charge introduced by the pCMF residue on the Cc surface prevents cation exclusion between the proteins' redox active sites, thereby enabling charge screening in this confined interface and disrupting the Gouy-Chapman conduit (Fig. 4). The effects are even stronger in simulations with phosphorylated residues, which bear high relevance as they are not yet experimentally accessible. Besides, we observe that the single molecule unbinding of

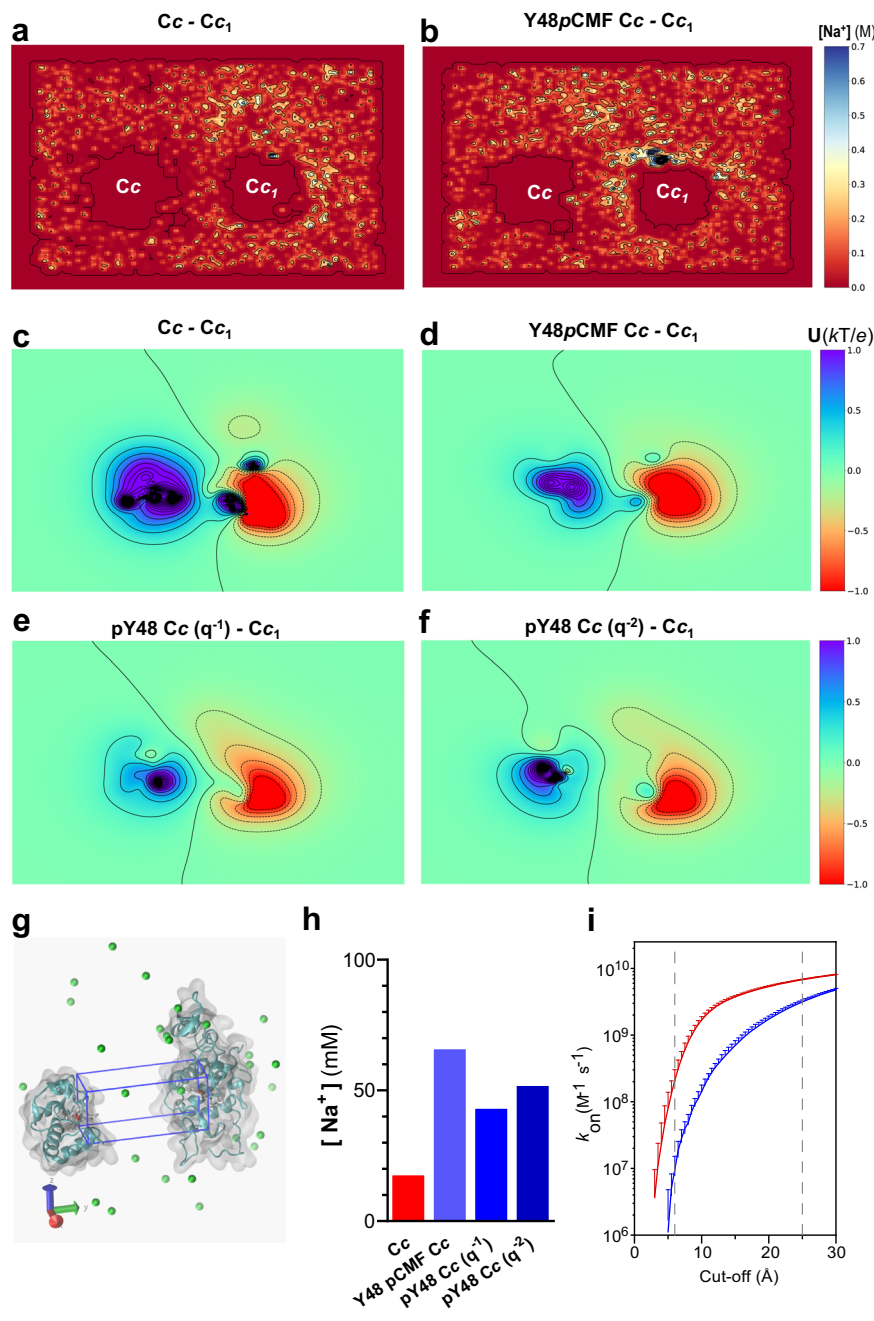


Fig. 4 | Molecular dynamics (MD) calculations of Cc_1 and Cc display an inter-protein Gouy-Chapman conduit that is disrupted by phosphorylation. **a, b** Side view of the averaged sodium concentration map (M) at the X-axis plane dissecting both Cc_1 - Cc redox active sites (Cc and Y48pCMF Cc , respectively) facing each other at 3.2 nm separation taking the most external hydrogen atoms from the $-CH_3$ distal pairs from each heme group, that is 4.2 nm taking the Fe-to-Fe distance. MD simulations were performed with explicit water (TIP3P solvent model) and 50 mM ionic concentration (NaCl) over 36 ns. Each contour line displays an increase of 0.15 M. **(c–f)** Side view of computed electrostatic potential with APBS⁷⁶ from -1 kT/e (red) to 1 kT/e (blue) for Cc_1 - Cc pairs: Cc_1 - Cc (**c**), Cc_1 -Y48pCMF Cc in silico (**d**), Cc_1 -pY48 Cc (O-phospho-L-tyrosine) with charge -1 (**e**) and Cc_1 -pY48 Cc (O-phospho-L-tyrosine) with charge -2 (**f**). Ion concentration is 50 mM, pH 6.5. Each contour line displays an increase of 0.2 kT/e. **g** Virtualization of the Cc_1 - Cc system in 3D. Representation of the prism (blue) used to calculate the average concentration of

sodium throughout the simulation. The image shows a single frame of the Cc_1 - Cc system depicting protein (cyan, translucent grey surface), heme groups (white with Iron atom in red), sodium ions (green spheres), and omitting water molecules. The closest backbone residues to the generated prism vertices are His18, Pro76, Lys79 and Ile85 of the Y48pCMF Cc , and Leu134, Leu94, Glu101 and Ala160 of Cc_1 . **h** Average sodium concentration over 36 ns in a 12.9 nm^3 volume prism (prism dimensions for $x, y, z = 15, 43, 20$ units) centered between both heme groups of Cc and Cc_1 for all systems. Volmap Tool Plugin 1.1 from VMD⁷⁵ was used. **i** Derivation of binding kinetics from the BD computations of Cc_1 - Cc (red) and Cc_1 -Y48pCMF Cc (blue) complexes. For each computation, two curves are represented, corresponding to 4 independent pair-distances criteria for reaction, as reported previously⁶⁵. Vertical lines correspond to the distances used as reaction criterion to estimate k_{on} and $k_{trigger}$ values. Source data are provided as a Source Data file.

Y48pCMF Cc from the redox partner Cc_1 occurs at higher forces (Fig. 3). These results are consistent with the higher binding affinities of phosphomimetic Cc compared to the wildtype in bulk experiments (Fig. 3g, Table 1) and BD calculations (Fig. 4i, Table 2).

Figure 5 recapitulates all these results and provides a mechanistic framework showing how phosphorylation of Cc alters several functions of this multifaceted protein involved in electron transport and cell fate. First, by shutting down its ability to exchange charge with

Table 2 | Analysis of brownian dynamics (BD) simulations for the Cc₁-Cc interaction

	Cc ₁ -Cc	Cc ₁ -Y48pCMF Cc
k_{on} (M ⁻¹ s ⁻¹) (0.6 nm)	9.50·10 ⁶ ± 7.90·10 ⁶	2.10·10 ⁸ ± 9.6·10 ⁷
$k_{trigger}$ (M ⁻¹ s ⁻¹) (2.5 nm)	3.20·10 ⁹ ± 8.6·10 ⁷	6.80·10 ⁹ ± 1.4·10 ⁸

Estimated association rate at contact level (k_{on}) and at the cut-off distance of 2.5 nm ($k_{trigger}$). The errors reported correspond to the standard deviation.

Cc₁ (complex III) at long distances through the aqueous solution and in an electrochemically selective manner⁴. And second, by promoting a stronger contact with Cc₁ that disturbs the reversible binding found in equilibrium conditions (low forces) and likely reduces the turnover of molecules at complex III. In this scenario, even small amounts of phosphorylated Cc will lead to one of them being stuck at complex III and effectively preventing others from transferring charge. The dissociation constant (K_D) is lower for the Cc Y48pCMF variant, which must get closer to complex III than the wildtype in order to achieve similar current levels (due to the higher β of the former, see Fig. 1a). In this situation, the interaction forces (unbinding force, Fig. 3; binding affinity, Table 1 and Fig. 3g; association rate, Table 2 and Fig. 4i) are higher and thereby the overall turnover of Cc molecules is reduced, lowering the complex III activity (Supplementary Fig. 4). The higher conductance observed in the Y48pCMF variant compared to the WT species (Fig. 2c) might be caused by such closer interaction.

In conclusion, we have performed a multimodal study of the interaction between redox partners Cc and Cc₁ that covers single protein conductance and force measurements, bulk binding and biochemical assays, and molecular dynamics calculations. By studying a phosphomimetic mutation, we have focused on the impact of phosphorylation in all the observables and integrated the obtained results within the available biochemical evidence, aiming to provide a nanoscopic view and mechanistic framework that was lacking in this topic. Phosphorylation of Cc impairs electrochemically gated long-distance electron transport through the solution and disturbs the binding/unbinding equilibrium between the partners, strengthening their interaction. Calculations show that the cation exclusion volume that is established between the partners (Gouy-Chapman conduit) is disrupted by the negative charges introduced near the Cc redox site by phosphorylation and its experimental molecular mimics. These results allow a deeper understanding of the tradeoff between binding, transfer, and turnover that is established between redox protein partners in the respiratory ETC and provide mechanistic insights into the molecular sites that regulate cell signaling circuits.

Methods

Protein expression and purification

Escherichia coli (*E. coli*) BL21 (DE3) cells were transformed with pBTR1-WT plasmid—that contained the *CYCS* gene-coding for human Cc and, the *CYC3* gene of the yeast Cc heme lyase, required for the maturation of Cc—to recombinantly express *Homo sapiens* WT Cc for Surface Plasmon Resonance (SPR) experiments. For the expression of E104C mutant, used for Electrochemical Scanning Tunneling Microscope (EC-STM) and Atomic Force Microscopy-Force Spectroscopy (AFM-FS) measurements, pBTR-1 plasmid was mutated by replacing the GAA triplet corresponding to Glu104 by TGT, which codifies to cysteine residue. The primers for PCR were pBTR1-E104C fw (5-AAGGCGACGAAGTGTGATAAGGTACCA-3) and pBTR1-E104C rv (5-TGGTACCTTATCAACAGTTCGTCGCTT-3). For this purpose, one-step mutagenic PCR with Accusure™ DNA Polymerase (Bioline) was used following the manufacturer's instructions. The new plasmid, containing the mutated sequence, is designated as pBTR1-E104C. Expression and purification of both Cc species was carried out as previously described⁶⁸. Briefly, transformed bacteria were incubated

for 20 h at 150 rpm and 30 °C in 2.5 L standard lysogeny broth (LB) rich medium (10 g·L⁻¹ tryptone, 5 g·L⁻¹ yeast extract and 10 g·L⁻¹ NaCl), supplemented with 100 µg·mL⁻¹ ampicillin. Cells were harvested via centrifugation at 5000 x g for 10 min at 4 °C, resuspended in 10 mM tricine buffer pH 8.5 supplemented with cOmplete protease inhibitor cocktail (#11836145001, Roche), ruptured by sonication for 5 min, and then centrifuged at 14,000 x g for 60 min. The supernatant was loaded onto a Nuvia S column (#7324720, Biorad) and eluted with a 25 to 500 mM NaCl gradient in 10 mM tricine buffer pH 8.5. Phosphomimetic Y48pCMF Cc was expressed using the evolved tRNA synthetase technique, as previously described⁴¹. Briefly, *E. coli* BL21 (DE3) cells were co-transformed with either pBTR1-Y48AMBER or pBTR1-Y48AMBER/E104C, and pEVOL/pCMF/tRNA plasmids—which contains the unnatural tRNA/aminoacyl-tRNA synthetase pair that recognizes the pCMF—and were cultured for 20 h at 150 rpm and 30 °C in M9 minimal medium supplemented with 100 µg·mL⁻¹ ampicillin, 20 µg·mL⁻¹ chloramphenicol, 16.7 µg·mL⁻¹ δ -aminolevulinic acid hydrochloride and 263 µg·mL⁻¹ non-canonical amino acid pCMF. Protein expression was induced with 1 mM isopropyl- β -D-thiogalactoside and 0.02% arabinose. Cells were harvested by centrifugation and purified similarly as previously described for Cc⁴¹. The soluble domain of *Arabidopsis thaliana* Cc₁ was expressed and purified as previously described¹². Briefly, *E. coli* BL21 (DE3) cells were co-transformed with pET-Cc₁ and pEC86 plasmids (which constitutively express the eight cytochrome *c* maturation genes *ccmABCDEFGHIH*) to produce the soluble domain of Cc₁ (residues 64–265, Gene ID 834081). The cells were grown for 24 h at 150 rpm and 30 °C in 2 L of standard LB rich medium, supplemented with 50 µg·mL⁻¹ kanamycin, 12 µg·mL⁻¹ chloramphenicol and 16.7 µg·mL⁻¹ δ -aminolevulinic acid hydrochloride. Harvested cells were resuspended in 20 mM Tris-HCl buffer pH 8.0 supplemented with cOmplete protease inhibitor cocktail (#11836145001, Roche) and physically ruptured by sonication for 5 min. The supernatant was loaded onto a Nuvia Q column (#7324721, Biorad) and eluted with a 25 to 500 mM NaCl gradient in 20 mM Tris-HCl buffer pH 8.0. Fractions containing Cc₁ were further purified by size exclusion with a ENrich SEC 70 column (#7801070, Biorad). All protein samples were dialyzed against 10 mM sodium phosphate buffer at pH 6.5.

Electrochemical scanning tunneling microscopy-spectroscopy

Sample preparation. Atomically flat Au(111) single-crystal disks (10 mm diameter and 1 mm thickness, MaTeck) were flame annealed and electrochemically polished⁴⁵. The Au(111) electrodes were incubated with Cc₁ in sodium phosphate buffer 10 mM, pH = 6.5 at a 56 µM concentration. The EC-STM probes (Au wire 0.25 mm in diameter; GoodFellow) were insulated with Apiezon™⁴⁵, and were incubated with a 12.5 µM solution of either Cc (E104C) or Y48pCMF Cc (E104C), in sodium phosphate buffer 10 mM, pH = 6.5. All incubations were conducted overnight and at 4 °C.

EC-STM measurements. All experiments were performed with a PicoSPM microscope head and a PicoStat bipotentiostat (Agilent, USA) controlled by Dulcinea electronics (Nanotec Electronica, Spain) using the WSxM 4.13 software. A custom-made electrochemical liquid cell with a standard sample plate was used in four-electrode configuration with the STM Au(111) sample and probe as working electrodes, a 0.25 mm diameter Pt80/Ir20 wire as counter electrode and a miniaturized ultralow leakage membrane Ag/AgCl (SSC) reference electrode filled with 3 M KCl. The potentials of the Au(111) electrode sample (U_S) and EC-STM probe (U_P) were expressed against this reference. The electrochemical cell was cleaned with piranha solution (3:1 v/v solution of H₂SO₄ and H₂O₂) before each measurement. Caution: piranha solution is a strong oxidizer and a strong acid. It should be handled with extreme care, as it reacts violently with most organic materials. The experiments

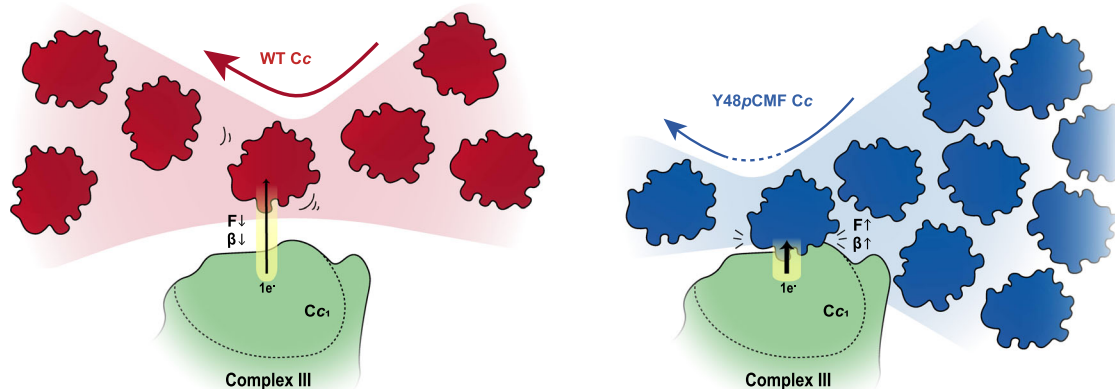


Fig. 5 | Proposed model showing how phosphorylation of cytochrome *c* promotes a closer contact with cytochrome *c*₁ and diminishes the turnover of molecules at complex III. (Left) WT cytochrome *c* (red) can receive electrons from cytochrome *c*₁ of complex III at long distances (low β). Overall turnover of cytochrome *c* molecules at complex III is high due to reversible binding in equilibrium conditions (low F). **(Right)** Compared to WT Cc (red), the dissociation constant (K_D) of the Y48pCMF variant (blue) is lower and it must get closer to complex III for

electron transfer (high β). In this situation, the interaction forces are higher (high F) and thereby the overall turnover of electron carriers is reduced. Conductance of the Y48pCMF variant is higher (right, thick black arrow), compared to that of the WT species (left, thin black arrow). Thus, phosphorylation of cytochrome *c* disrupts the long-distance electron transfer conduit (marked in yellow) previously observed in the wild-type protein⁶.

were performed in sodium phosphate buffer 50 mM (pH = 6.5) electrolyte solution, previously filtered through 0.02 μm diameter sterile membrane (Anotop) and degassed with nitrogen.

The Current versus distance (I - z) curves were acquired by setting an initial current set point of 0.4 nA, turning the feedback loop off, and recording the probe current at 12 $\text{nm}\cdot\text{s}^{-1}$ during probe retraction along 15 nm (20 samples per point, 1024 points) at a constant bias ($U_{\text{bias}} = U_P - U_S$). At least 2 independent experiments were conducted in each case. For each independent experiment, a total of 150 curves (20 samples per point, 1024 points) were recorded. The data were treated with the custom-generated MATLAB code (The MATHWORKS, Inc.) previously reported⁴.

For static blinking experiments, a NI-DAQmx and BNC-2110 LabVIEW setup was used for data acquisition, LabVIEW software was used for data treatment. The STM probe is set at a fixed current set point from the sample, and at a constant bias, and the feedback is turned off after a period of mechanical stabilization. Current versus time traces are then recorded in captures of few seconds during several hours. Current blinks are observed in the current transient in the form of telegraphic noise (Fig. 2a). At least 2 independent experiments were conducted in each case. The current is transformed to conductance values using $G = I_{\text{blink}}/U_{\text{bias}}$. Up to a hundred blinks are used to build 2D-blinking maps.

The data were analyzed with OriginPro 8.5.0 SRI (OriginLab Corp.). n indicates the sample size in all cases. Errors are indicated as standard deviation of the mean.

Atomic force microscopy-force spectroscopy

Sample preparation. Cc₁ was immobilized on atomically flat Au(111) single-crystal disks (10 mm diameter, 1 mm thickness, MaTeck). The Au(111) disks were electrochemically polished⁴⁵ and flame annealed, cooled under a nitrogen flow and then incubated with a 56 μM solution of Cc₁ in sodium phosphate buffer 10 mM, pH 6.5 within a humid environment, overnight and at 4 °C.

AFM probes preparation. We used V-shaped Si₃N₄ cantilevers (Bruker AFM Probes, Camarillo, CA) having a nominal spring constant of 0.06 $\text{N}\cdot\text{m}^{-1}$ with either silicon (SNL probes) or Au-coated (NPG probes) tips.

Au-coated probes were placed on a PDMS surface and incubated with a 25 μL drop of a 26 μM solution of Cc (E104C) or Y48pCMF Cc

(E104C) in sodium phosphate buffer 10 mM, pH 6.5. Incubations were performed at 4 °C overnight in a humid environment.

Silicon probes were first treated for 10 minutes in a UV/Ozone ProCleaner™ (BioForce Nanosciences). Then, the probes were aminofunctionalized in atmosphere of 3-aminopropyl)triethoxysilane (APTES) and triethylamine (TEA). For this, the probes were placed inside the desiccator previously flooded with N₂ gas to remove air and moisture. Two small plastic containers with 45 μL of APTES and 15 μL of TEA, separately, were placed close to the probes (on a clean inert surface) and vacuum was on for 5 min. After 1.5 h, the APTES and TEA container were removed, and vacuum was restored. The probes were left in the desiccator overnight at room temperature. The probes were then rinsed with chloroform (2x) and ethanol (2x) and dried under a gentle N₂ flow. When the tips were not used immediately, they were stored in a desiccator under Ar atmosphere. The AFM probes were then placed in glass wells filled with 0.5 ml solution of 1 $\text{mg}\cdot\text{mL}^{-1}$ heterobifunctional PEG ($n = 27$) (Mal-PEG₂₇-NHS, *O*-[*N*-(3-maleimidopropionyl)aminoethyl]-*O'*-[3-(*N*-succinimidylxy)-3-oxopropyl]heptacosaehtylene glycol, Sigma-Aldrich) and 5 μL TEA in chloroform and left for 2 h. The probes were then rinsed with chloroform (2x), ethanol (2x) and MilliQ water and dried under a gentle N₂ flow. The probes were placed onto a PDMS surface and incubated with a 25 μL drop of a 26 μM solution of Cc (E104C) or Y48pCMF Cc (E104C) in sodium phosphate buffer 10 mM, pH 6.5. Incubations were performed at 4 °C overnight in a humid environment.

AFM-FS measurements. Force-separation curves were measured with either an MFP3D AFM (Asylum Research, Oxford Instruments) or a NanoWizard 3 BioScience AFM (JPK Instruments, Bruker Nano GmbH) at room temperature and under liquid environment (sodium phosphate buffer 50 mM, pH 6.5). After having measured the sensitivity ($V\cdot\text{m}^{-1}$), the cantilever spring constants were individually calibrated by using the equipartition theorem (thermal noise routine)⁶⁹. Force-separation curves were recorded by approaching and retracting the AFM tip at constant velocity (0.5 to 4 $\mu\text{m}\cdot\text{s}^{-1}$) and in the force map mode over an area of 3 \times 3 μm^2 . The maximum applied (contact) force in each cycle was set to 300 pN. At least two independent experiments were conducted in each case. AFM data were acquired and treated using the AFM software and analyzed with OriginPro 8.5.0 SRI (OriginLab Corp.). Errors are indicated as the standard deviation of the mean.

Surface plasmon resonance SPRI

Cc interaction to Cc₁ was assayed by SPR using a CS SPRI-Biochip™ (HORIBA Scientific) and a SPRI-Plex II™ system (HORIBA Scientific), as previously described with minor modifications⁷⁰. Briefly, Cc₁ direct amine immobilization onto the biochip was achieved by deposition of 10 and 15 μM solution drops on the surface and rabbit serum albumin (Sigma-Aldrich) was used as control at reference spots. The binding assays were performed at 298 K in 10 mM sodium phosphate buffer, pH 6.5. WT or Y48pCMF Cc were flowed at various concentrations (from 2.5 to 10 μM) over the modified surface with Cc₁ at 50 μL·min⁻¹ rate. The signals from the reference spot surface were subtracted in every sensogram. The data were analyzed and fitted to a one-to-one binding model adapted from Bowles *et al.*⁷¹, with Origin 2018 (OriginLab Corporation).

Cytochrome bc₁ complex activity

The ability of WT and Y48pCMF Cc variants to act as electron acceptor of cytochrome bc₁ complex (complex III) was tested with mammalian mitochondria extracted from HeLa cells. HeLa cells were cultured in Dulbecco's modified Eagle's medium (DMEM; Sigma-Aldrich) supplemented with 10% heat-inactivated fetal bovine serum (FBS; Sigma-Aldrich), 2 mM L-glutamine (Sigma-Aldrich), 100 U·mL⁻¹ streptomycin (Sigma-Aldrich) and 100 μg·mL⁻¹ penicillin (Sigma-Aldrich). Mitochondria were isolated from HeLa cells as previously described and stored at -80 °C in 10 mM Tris-MOPS, 1 mM EGTA/Tris, 200 mM sucrose pH 7.4⁷². Complex III activity was measured spectrophotometrically (Varioskan™ LUX microplate reader, Thermo Scientific™) using the commercial mitochondrial complex III activity kit from Abcam (ab287844), according to the manufacturer's instructions. Net complex III activity was calculated by comparing the Cc reduction in the presence and absence of Antimycin A, a complex III specific inhibitor.

Molecular dynamics simulations

The initial model of the Cc and Cc₁ proteins was done essentially as described by Lagunas *et al.*⁴, built from the PDB structure 3CX5⁷³, using the Multiseq plugin⁷⁴ of the VMD program⁷⁵. The two proteins were separated 3.2 nm along one axis, taking the most external hydrogen atom from the -CH₃ distal pairs from each heme group, that is 4.2 nm taking the Fe-to-Fe distance. The molecular dynamics (MD) simulation was set up with the program LEaP included in the Amber suite of programs⁷⁶ and the ff99SB protein force field. The titratable residues were modeled in the corresponding protonation state at pH 6.5, which was further checked by analysis of their intermolecular interactions. The AMBER parameters database (<http://research.bmh.manchester.ac.uk/bryce/amber>) was used for the heme parameters, considering RESP charges for the reduced and oxidized cases from Autenrieth *et al.*⁷⁷. Values from the same reference were used to parametrize the charges of the interacting residues with the heme groups, His18/44 and Met80/166 from Cc/Cc₁ respectively. Explicit TIP3P water molecules were used for solvation⁷⁸, and the system was neutralized with 33/35 sodium/chlorine atoms, in addition to the 33 NaCl molecules to reproduce a concentration of 50 mM. The final system contained 105541 atoms. Amber14⁷⁹ was used for the MD simulations. A restraint on the residues 1–15 for Cc₁ and 97–104 for Cc was applied to model the experimental situation of Cys10 and Cys104, respectively, immobilized on the gold surfaces. A thermal equilibration to 300 K was first done, followed by the equilibration dynamics in the NPT ensemble for 36 ns. We used the SHAKE algorithm, with an integration time step of 2 fs. To obtain the equipotential surfaces, APBS electrostatics calculations⁸⁰ were done in the postprocessing step. Average ions and water concentration maps and number density prism volumes were obtained with the Volmap Plugin 1.1. Matplotlib⁸¹ and VMD⁷⁵ were used to draw the figures.

Brownian dynamics simulations

Brownian dynamics (BD) computations were carried out and analyzed using the SDA-flex 7.1 software package⁸². The force-field grids used in BD included all electrostatics and desolvation^{65,83} grids. Charges were obtained from PQR files extracted from each MD trajectory. Diffusion constants were computed using the script ARO⁸⁴, in the VMD tcl-tk console. Electrostatic grids were generated for every conformer with APBS 3.0⁸⁵. All simulations were carried out at 100 mM ionic strength. In total, 20 structures of Cc₁ and other 20 of Cc were used as input. For *k_{on}* computations, each of the 20 Cc₁ molecules were treated as targets in separate computations and set in the coordinate origin, whereas the 20 conformations of Cc were used as input for Monte-Carlo conformation exchange during the simulation of their diffusion. Conformational exchange was allowed every 2.5 ns. A total of 200,000 diffusion trajectories (20 × 10,000) were then computed. Origin 2019b (Originlab) was used for statistical analysis and data representation.

Reporting summary

Further information on research design is available in the Nature Portfolio Reporting Summary linked to this article.

Data availability

All the data generated in this study are available within the main text and the Supplementary Information file; source data are provided in the Source Data file. Data is also available from the corresponding author upon request. Source data are provided with this paper.

Code availability

The source code used to compute the presented results can be obtained from the electronic supplementary material available at: <https://www.nature.com/articles/s41467-018-07499-x> (reference 4).

References

1. McLendon, G. & Hake, R. Interprotein electron transfer. *Chem. Rev.* **92**, 481–490 (1992).
2. Crowley, P. B. & Carrondo, M. A. The architecture of the binding site in redox protein complexes: Implications for fast dissociation. *Proteins Struct. Funct. Bioinforma.* **55**, 603–612 (2004).
3. Bendall, D. S., Schlarb-Ridley, B. G. & Howe, C. J. Transient Interactions Between Soluble Electron Transfer Proteins. The Case of Plastocyanin and Cytochrome f BT - Bioenergetic Processes of Cyanobacteria: From Evolutionary Singularity to Ecological Diversity. in (eds. Peschek, G. A., Obinger, C. & Renger, G.) 541–571 (Springer Netherlands, 2011). https://doi.org/10.1007/978-94-007-0388-9_19.
4. Lagunas, A. *et al.* Long distance electron transfer through the aqueous solution between redox partner proteins. *Nat. Commun.* **9**, 3–9 (2018).
5. Pérez-Mejías, G., Díaz-Quintana, A., Guerra-Castellano, A., Díaz-Moreno, I. & De la Rosa, M. A. Novel insights into the mechanism of electron transfer in mitochondrial cytochrome c. *Coord. Chem. Rev.* **450**, 214233 (2022).
6. Soltys, B. J., Andrews, D. W., Jemmerson, R. & Gupta, R. S. Cytochrome-c localizes in secretory granules in pancreas and anterior pituitary. *Cell Biol. Int.* **25**, 331–338 (2001).
7. González-Arzola, K. *et al.* New moonlighting functions of mitochondrial cytochrome c in the cytoplasm and nucleus. *FEBS Lett.* **593**, 3101–3119 (2019).
8. Hüttemann, M. *et al.* The multiple functions of cytochrome c and their regulation in life and death decisions of the mammalian cell: From respiration to apoptosis. *Mitochondrion* **11**, 369–381 (2011).
9. D'Herde, K. *et al.* Ultrastructural localization of cytochrome c in apoptosis demonstrates mitochondrial heterogeneity. *Cell Death Differ.* **7**, 331–337 (2000).

10. Alvarez-Paggi, D. et al. Multifunctional cytochrome c: Learning new tricks from an old dog. *Chem. Rev.* **117**, 13382–13460 (2017).
11. Moreno-Beltrán, B. et al. Cytochrome c1 exhibits two binding sites for cytochrome c in plants. *Biochim. Biophys. Acta - Bioenerg.* **1837**, 1717–1729 (2014).
12. Moreno-Beltrán, B. et al. Respiratory complexes III and IV can each bind two molecules of cytochrome c at low ionic strength. *FEBS Lett.* **589**, 476–483 (2015).
13. Martínez-Fábregas, J. et al. New Arabidopsis thaliana cytochrome c partners: a look into the elusive role of cytochrome c in programmed cell death in plants. *Mol. Cell. Proteom.* **12**, 3666–3676 (2013).
14. Martínez-Fábregas, J. et al. Structural and functional analysis of novel human cytochrome c targets in apoptosis. *Mol. Cell. Proteom.* **13**, 1439–1456 (2014).
15. Martínez-Fábregas, J., Díaz-Moreno, I., González-Arzola, K., Díaz-Quintana, A. & De la Rosa, M. A. A common signalosome for programmed cell death in humans and plants. *Cell Death Dis.* **5**, e1314–e1314 (2014).
16. González-Arzola, K. et al. Structural basis for inhibition of the histone chaperone activity of SET/TAF- β by cytochrome c. *Proc. Natl Acad. Sci.* **112**, 9908–9913 (2015).
17. González-Arzola, K. et al. Histone chaperone activity of Arabidopsis thaliana NRP1 is blocked by cytochrome c. *Nucleic Acids Res.* **45**, 2150–2165 (2017).
18. Elena-Real, C. A. et al. Cytochrome c speeds up caspase cascade activation by blocking 14-3-3 ϵ -dependent Apaf-1 inhibition. *Cell Death Dis.* **9**, 365 (2018).
19. Elena-Real, C. A. et al. Proposed mechanism for regulation of H₂O₂-induced programmed cell death in plants by binding of cytochrome c to 14-3-3 proteins. *Plant J.* **106**, 74–85 (2021).
20. Rivero-Rodríguez, F. et al. Inhibition of the PP2A activity by the histone chaperone ANP32B is long-range allosterically regulated by respiratory cytochrome c. *Redox Biol.* **43**, 101967 (2021).
21. Zhao, R.-Z., Jiang, S., Zhang, L. & Yu, Z.-B. Mitochondrial electron transport chain, ROS generation and uncoupling (Review). *Int. J. Mol. Med.* **44**, 3–15 (2019).
22. Díaz-Quintana, A., Pérez-Mejías, G., Guerra-Castellano, A., De la Rosa, M. A. & Díaz-Moreno, I. Wheel and deal in the mitochondrial inner membranes: The tale of cytochrome c and cardiolipin. *Oxid. Med. Cell. Longev.* **2020**, 6813405 (2020).
23. Garrido, C. et al. Mechanisms of cytochrome c release from mitochondria. *Cell Death Differ.* **13**, 1423–1433 (2006).
24. Ascenzi, P. et al. Cardiolipin–cytochrome c complex: Switching cytochrome c from an electron-transfer shuttle to a myoglobin- and a peroxidase-like heme-protein. *IUBMB Life* **67**, 98–109 (2015).
25. Bergstrom, C. L., Beales, P. A., Lv, Y., Vanderlick, T. K. & Groves, J. T. Cytochrome c causes pore formation in cardiolipin-containing membranes. *Proc. Natl Acad. Sci.* **110**, 6269–6274 (2013).
26. Petrosillo, G., Ruggiero, F. M. & Paradies, G. Role of reactive oxygen species and cardiolipin in the release of cytochrome c from mitochondria. *FASEB J.* **17**, 2202–2208 (2003).
27. Li, P. et al. Cytochrome c and dATP-dependent formation of Apaf-1/Caspase-9 complex initiates an apoptotic protease cascade. *Cell* **91**, 479–489 (1997).
28. Zou, H., Li, Y., Liu, X. & Wang, X. An APAF-1-Cytochrome c multimeric complex is a functional apoptosome that activates procaspase-9. *J. Biol. Chem.* **274**, 11549–11556 (1999).
29. Hannibal, L. et al. Alternative conformations of cytochrome c: Structure, function, and detection. *Biochemistry* **55**, 407–428 (2016).
30. Guerra-Castellano, A. et al. Post-translational modifications of cytochrome c in cell life and disease. *Int. J. Mol. Sci.* **21**, 8483 (2020).
31. Kalpage, H. A. et al. Cytochrome c phosphorylation: Control of mitochondrial electron transport chain flux and apoptosis. *Int. J. Biochem. Cell Biol.* **121**, 105704 (2020).
32. Hüttemann, M., Lee, I., Grossman, L. I., Doan, J. W. & Sanderson, T. H. Phosphorylation of mammalian cytochrome c and cytochrome c oxidase in the regulation of cell destiny: respiration, apoptosis, and human disease. *Adv. Exp. Med. Biol.* **748**, 237–264 (2012).
33. Taddei, M. L., Pardella, E., Pranzini, E., Raugei, G. & Paoli, P. Role of tyrosine phosphorylation in modulating cancer cell metabolism. *Biochim. Biophys. Acta - Rev. Cancer* **1874**, 188442 (2020).
34. Lim, W. A. & Pawson, T. Phosphotyrosine signaling: Evolving a new cellular communication system. *Cell* **142**, 661–667 (2010).
35. Yu, H., Lee, I., Salomon, A. R., Yu, K. & Hüttemann, M. Mammalian liver cytochrome c is tyrosine-48 phosphorylated in vivo, inhibiting mitochondrial respiration. *Biochim. Biophys. Acta - Bioenerg.* **1777**, 1066–1071 (2008).
36. De Rocco, D. et al. Mutations of cytochrome c identified in patients with thrombocytopenia THC4 affect both apoptosis and cellular bioenergetics. *Biochim. Biophys. Acta - Mol. Basis Dis.* **1842**, 269–274 (2014).
37. Fan, C., Ip, K. & Söll, D. Expanding the genetic code of *Escherichia coli* with phosphotyrosine. *FEBS Lett.* **590**, 3040–3047 (2016).
38. Pérez-Mejías, G. et al. Exploring protein phosphorylation by combining computational approaches and biochemical methods. *Comput. Struct. Biotechnol. J.* **18**, 1852–1863 (2020).
39. Pecina, P. et al. Phosphomimetic substitution of cytochrome c tyrosine 48 decreases respiration and binding to cardiolipin and abolishes ability to trigger downstream Caspase activation. *Biochemistry* **49**, 6705–6714 (2010).
40. García-Heredia, J. M. et al. Tyrosine phosphorylation turns alkaline transition into a biologically relevant process and makes human cytochrome c behave as an anti-apoptotic switch. *JBC J. Biol. Inorg. Chem.* **16**, 1155–1168 (2011).
41. Guerra-Castellano, A. et al. Mimicking tyrosine phosphorylation in human cytochrome c by the evolved tRNA synthetase technique. *Chem. – A Eur. J.* **21**, 15004–15012 (2015).
42. Moreno-Beltrán, B. et al. Structural basis of mitochondrial dysfunction in response to cytochrome c phosphorylation at tyrosine 48. *Proc. Natl Acad. Sci.* **114**, E3041 LP–E3043050 (2017).
43. Amdursky, N. et al. Solid-state electron transport via cytochrome c depends on electronic coupling to electrodes and across the protein. *Proc. Natl Acad. Sci.* **111**, 5556–5561 (2014).
44. Güell, A. G., Díez-Pérez, I., Gorostiza, P. & Sanz, F. Preparation of reliable probes for electrochemical tunneling spectroscopy. *Anal. Chem.* **76**, 5218–5222 (2004).
45. Artés, J. M., Díez-Pérez, I. & Gorostiza, P. Transistor-like behavior of single metalloprotein junctions. *Nano Lett.* **12**, 2679–2684 (2012).
46. Heering, H. A., Wiertz, F. G. M., Dekker, C. & de Vries, S. Direct immobilization of native yeast iso-1 cytochrome c on bare gold: fast electron relay to redox enzymes and zeptomole protein-film voltammetry. *J. Am. Chem. Soc.* **126**, 11103–11112 (2004).
47. Bortolotti, C. A. et al. The redox chemistry of the covalently immobilized native and low-pH forms of yeast iso-1-cytochrome c. *J. Am. Chem. Soc.* **128**, 5444–5451 (2006).
48. Maity, H., Maity, M. & Walter Englander, S. How cytochrome c folds, and why: submolecular foldon units and their stepwise sequential stabilization. *J. Mol. Biol.* **343**, 223–233 (2004).
49. Battistuzzi, G., Borsari, M., Cowan, J. A., Ranieri, A. & Sola, M. Control of cytochrome c redox potential: Axial ligation and protein environment effects. *J. Am. Chem. Soc.* **124**, 5315–5324 (2002).
50. Monari, S. et al. The impact of urea-induced unfolding on the redox process of immobilised cytochrome c. *JBC J. Biol. Inorg. Chem.* **15**, 1233–1242 (2010).

51. Casalini, S. et al. Electron transfer and electrocatalytic properties of the immobilized methionine80alanine cytochrome c variant. *J. Phys. Chem. B* **112**, 1555–1563 (2008).
52. Artés, J. M., López-Martínez, M., Díez-Pérez, I., Sanz, F. & Gorostiza, P. Conductance switching in single wired redox proteins. *Small* **10**, 2537–2541 (2014).
53. Ruiz, M. P. et al. Bioengineering a single-protein junction. *J. Am. Chem. Soc.* **139**, 15337–15346 (2017).
54. Rief, M., Oesterhelt, F., Heymann, B. & Gaub, H. E. Single molecule force spectroscopy on polysaccharides by atomic force microscopy. *Science* **275**, 1295–1297 (1997).
55. Oesterhelt, F., Rief, M. & Gaub, H. E. Single molecule force spectroscopy by AFM indicates helical structure of poly(ethylene-glycol) in water. *N. J. Phys.* **1**, 6 (1999).
56. Ma, Z. et al. TCR triggering by pmhc ligands tethered on surfaces via poly(ethylene glycol) depends on polymer length. *PLoS One* **9**, e112292 (2014).
57. Evans, E. & Ritchie, K. Dynamic strength of molecular adhesion bonds. *Biophys. J.* **72**, 1541–1555 (1997).
58. Merkel, R., Nassoy, P., Leung, A., Ritchie, K. & Evans, E. Energy landscapes of receptor–ligand bonds explored with dynamic force spectroscopy. *Nature* **397**, 50–53 (1999).
59. Evans, E. Probing the relation between force - Lifetime - and chemistry in single molecular bonds. *Annu. Rev. Biophys. Biomol. Struct.* **30**, 105–128 (2001).
60. Friddle, R. W., Noy, A. & De Yoreo, J. J. Interpreting the widespread nonlinear force spectra of intermolecular bonds. *Proc. Natl Acad. Sci.* **109**, 13573–13578 (2012).
61. Auletta, T. et al. β -Cyclodextrin Host–Guest Complexes Probed under Thermodynamic Equilibrium: Thermodynamics and AFM Force Spectroscopy. *J. Am. Chem. Soc.* **126**, 1577–1584 (2004).
62. Bell, G. I. Models for specific adhesion of cells to cells. *Science* **200**, 618–627 (1978).
63. Dettmann, W. et al. Differences in zero-force and force-driven kinetics of ligand dissociation from β -galactoside-specific proteins (plant and animal lectins, immunoglobulin G) monitored by plasmon resonance and dynamic single molecule force microscopy. *Arch. Biochem. Biophys.* **383**, 157–170 (2000).
64. Farrance, O. E. et al. A Force-activated trip switch triggers rapid dissociation of a colicin from its immunity protein. *PLoS Biol.* **11**, e1001489 (2013).
65. Elcock, A. H., Gabdouliline, R. R., Wade, R. C. & McCammon, J. A. Computer simulation of protein-protein association kinetics: acetylcholinesterase-fasciculin. *J. Mol. Biol.* **291**, 149–162 (1999).
66. Nault, L. et al. Electrochemical atomic force microscopy imaging of redox-immunomarked proteins on native potyvirus: From Sub-particle to single-protein resolution. *ACS Nano* **9**, 4911–4924 (2015).
67. Pobelov, I. V. et al. Electrochemical current-sensing atomic force microscopy in conductive solutions. *Nanotechnology* **24**, 115501 (2013).
68. Guerra-Castellano, A., Díaz-Moreno, I., Velázquez-Campoy, A., De la Rosa, M. A. & Díaz-Quintana, A. Structural and functional characterization of phosphomimetic mutants of cytochrome c at threonine 28 and serine 47. *Biochim. Biophys. Acta - Bioenerg.* **1857**, 387–395 (2016).
69. Hutter, J. L. & Bechhoefer, J. Calibration of atomic-force microscope tips. *Rev. Sci. Instrum.* **64**, 1868–1873 (1993).
70. Pérez-Mejías, G. et al. Physical contact between cytochrome c1 and cytochrome c increases the driving force for electron transfer. *Biochim. Biophys. Acta - Bioenerg.* **1861**, 148277 (2020).
71. Bowles, M. R., Hall, D. R., Pond, S. M. & Winzor, D. J. Studies of protein interactions by biosensor technology: An alternative approach to the analysis of sensorgrams deviating from pseudo-first-order kinetic behavior. *Anal. Biochem.* **244**, 133–143 (1997).
72. Frezza, C., Cipolat, S. & Scorrano, L. Organelle isolation: functional mitochondria from mouse liver, muscle and cultured fibroblasts. *Nat. Protoc.* **2**, 287–295 (2007).
73. Solmaz, S. R. N. & Hunte, C. Structure of complex III with bound cytochrome c in reduced state and definition of a minimal core interface for electron transfer. *J. Biol. Chem.* **283**, 17542–17549 (2008).
74. Roberts, E., Eargle, J., Wright, D. & Luthey-Schulten, Z. MultiSeq: Unifying sequence and structure data for evolutionary analysis. *BMC Bioinforma.* **7**, 382 (2006).
75. Humphrey, W., Dalke, A. & Schulten, K. VMD: Visual molecular dynamics. *J. Mol. Graph.* **14**, 33–38 (1996).
76. Pearlman, D. A. et al. AMBER, a package of computer programs for applying molecular mechanics, normal mode analysis, molecular dynamics and free energy calculations to simulate the structural and energetic properties of molecules. *Comput. Phys. Commun.* **91**, 1–41 (1995).
77. Autenrieth, F., Tajkhorshid, E., Baudry, J. & Luthey-Schulten, Z. Classical force field parameters for the heme prosthetic group of cytochrome c. *J. Comput. Chem.* **25**, 1613–1622 (2004).
78. Jorgensen, W. L., Chandrasekhar, J., Madura, J. D., Impey, R. W. & Klein, M. L. Comparison of simple potential functions for simulating liquid water. *J. Chem. Phys.* **79**, 926 (1983).
79. Case, D. A. et al. AMBER14. *AMBER 14* (2014).
80. Unni, S. et al. Web servers and services for electrostatics calculations with APBS and PDB2PQR. *J. Comput. Chem.* **32**, 1488–1491 (2011).
81. Hunter, J. D. Matplotlib: A 2D graphics environment. *Comput. Sci. Eng.* **9**, 90–95 (2007).
82. Gabdouliline, R. R. & Wade, R. C. Brownian dynamics simulation of protein–protein diffusional encounter. *Methods* **14**, 329–341 (1998).
83. Gabdouliline, R. R. & Wade, R. C. On the contributions of diffusion and thermal activation to electron transfer between phormidium laminosum plastocyanin and cytochrome *f*: Brownian dynamics simulations with explicit modeling of nonpolar desolvation interactions and electron transfer event. *J. Am. Chem. Soc.* **131**, 9230–9238 (2009).
84. Díaz-Moreno, I., Muñoz-López, F. J., Frutos-Beltrán, E., De la Rosa, M. A. & Díaz-Quintana, A. Electrostatic strain and concerted motions in the transient complex between plastocyanin and cytochrome *f* from the cyanobacterium *Phormidium laminosum*. *Bioelectrochemistry* **77**, 43–52 (2009).
85. Baker, N. A., Sept, D., Joseph, S., Holst, M. J. & McCammon, J. A. Electrostatics of nanosystems: Application to microtubules and the ribosome. *Proc. Natl Acad. Sci.* **98**, 10037–10041 (2001).

Acknowledgements

This research received funding from the European Union Research and Innovation Programme Horizon 2020 – HBP SG3 (945539) to P.G., DEEPER (ICT-36-2020-101016787) to P.G., Ministry of Science and Innovation (Grants PID2021-126663NB-I00 to I.D.-M., PID2019-111493RB-I00 to P.G., PGC2018-096049-B-I00 to I.D.-M., CTQ2015-66194-R to A.L. and M.I.G., and PID2020-118893GB-I00 to C.R.), the Spanish Structures of Excellence María de Maeztu (MDM-2017-0767 to C.R.), Fonds Européen de Développement Économique et Régional (FEDER) funds, Agency for Management of University and Research Grants/Generalitat de Catalunya (CERCA Programme, (2017-SGR-1079 to J.S., 2017-SGR-1442 to P.G. and 2017-SGR-1189 to C.R.), Andalusian Government (BIO-198 to I.D.-M., US-1254317 to I.D.-M., US-1257019 to M.A.R., P18-FR-3487 to I.D.-M., and P18-HO-4091 to I.D.-M., US/JUNTA/FEDER, UE), University of Seville (VI PPIT to I.D.-M.) and the Ramón Areces Foundation (2021-2024 to I.D.-M.).

The project CECH, 001-P-001682 to P.G. is co-financed by the European Union Regional Development Fund within the framework of the ERDF Operational Program of Catalonia 2014-2020 with a grant of 50% of total eligible cost. G.P.-M. was awarded a PhD fellowship from the Spanish Ministry of Education, Culture and Sport (FPU17/04604). A.L., M.I.G., J.S., and P.G. were supported by the Biomedical Research Networking Center (CIBER), Spain (CB06/01/0055 and CB06/01/0081). CIBER is an initiative funded by the VI National R&D&i Plan 2008-2011, Iniciativa Ingenio 2010, Consolider Program, CIBER Actions, and the Instituto de Salud Carlos III, with the support of the European Regional Development Fund (ERDF). This work was supported by grants. The authors also acknowledge Dr. Albert Cortijos Aragonès and Jessica Sierra Agudelo for help with the EC-STM blinking measurements and data analysis, and Manuel López Ortiz for technical assistance. We also thankfully acknowledge the computer resources at CTE-Power and the technical support provided by the Red Española de Supercomputación-Barcelona Supercomputing Center.

Author contributions

P.G. and A.L. designed the ECSTM experiments and A.L. performed the ECSTM experiments and data analyses; M.I.G. designed the AFM-FS experiments and M.I.G., L.C.-F. and S.O.-T. performed the AFM-FS experiments and data analyses; I.D.-M. and M.A. de la R. discussed the experiments and designed protein production, SPRi and Complex III activity experiments and A.G.-C. and G.P.-M. produced and purified the proteins, G.P.-M. performed the SPRi and Complex III activity experiments; P.G. and C.R. designed the MD experiments, and A.M.J.G. and A.N.-H. performed the simulations. A.D.-Q. performed the Brownian dynamics simulations. A.L., M.I.G., I.D.-M. and P.G. wrote the paper with contributions from A.M.J.G., G.P.-M., A.N.-H., A.G.-C., M.A. de la R., C.R., and J.S.; M.I.G. and A.L. contributed equally.

Competing interests

The authors declare no competing interests.

Additional information

Supplementary information The online version contains supplementary material available at <https://doi.org/10.1038/s41467-022-34809-1>.

Correspondence and requests for materials should be addressed to Carme Rovira, Irene Díaz-Moreno, Pau Gorostiza, Marina I. Giannotti or Anna Lagunas.

Peer review information *Nature Communications* thanks Naoki Matsuda and the other, anonymous, reviewer(s) for their contribution to the peer review of this work. Peer reviewer reports are available.

Reprints and permissions information is available at <http://www.nature.com/reprints>

Publisher's note Springer Nature remains neutral with regard to jurisdictional claims in published maps and institutional affiliations.

Open Access This article is licensed under a Creative Commons Attribution 4.0 International License, which permits use, sharing, adaptation, distribution and reproduction in any medium or format, as long as you give appropriate credit to the original author(s) and the source, provide a link to the Creative Commons license, and indicate if changes were made. The images or other third party material in this article are included in the article's Creative Commons license, unless indicated otherwise in a credit line to the material. If material is not included in the article's Creative Commons license and your intended use is not permitted by statutory regulation or exceeds the permitted use, you will need to obtain permission directly from the copyright holder. To view a copy of this license, visit <http://creativecommons.org/licenses/by/4.0/>.

© The Author(s) 2022